

DOI: -

Comparison of Two Different CAA Methods for the Prediction of Far-Field Noise from Heated and Unheated Jets

Jens Trümner and Christian Mundt

Thermodynamics Institute, Bundeswehr University Munich

Werner-Heisenberg-Weg 39, 85577 Neubiberg, Germany, jens.truemner@unibw.de

Abstract

Two set-points of the Acoustic Reference Nozzle 2 experiment, representing an unheated and a heated subsonic jet, are investigated numerically. The far-field noise spectra are calculated using two different CAA approaches. The first method is based on scale-resolving simulations (SRS). It exhibits a low degree of modeling and is therefore universal but expensive. The second method processes steady RANS data, which makes it an interesting tool for industrial applications. For the unheated jet the RANS based method produces excellent results, whereas the SRS over-predicts the sound pressure levels due to errors in the extrapolation to the far-field. Since only a source model for cold jets is utilized, the sound pressure levels for the heated jet are too low with the RANS based model. Here, the SRS results are closer to the microphone measurements, especially in the downstream direction, where the contribution from large-scale structures predominates the extrapolation errors.

1. Introduction

With the great success of civil jet planes after the second world war the problem of aerodynamically generated noise became obvious. The development of bypass engines could significantly reduce jet noise emissions by lowering the jet velocity and reducing velocity and temperature gradients between the highly energetic core flow and the surrounding air. This in turn decreased the degree of turbulence known to be one important source of jet noise. A further improvement could be achieved by mixing core and bypass flow together before they are expanded through a common nozzle. Thereby, the maximum temperature and thus the velocity at the nozzle exit is further decreased.

To understand and improve the jet noise characteristics of nozzle systems a variety of approaches were developed. After Lighthill's⁸ theoretical work on aerodynamically generated noise and acoustic analogies most of the findings were achieved experimentally. Tam et al.²² investigated a large number of NASA experiments on axis-symmetric jets and identified two universal noise spectra. One less directed from fine-scale turbulence (G-spectrum) and one downstream directed from instability wave radiation (F-spectrum). Based on mean flow and turbulence quantities, Tam and Auriant²¹ (T&A) proposed a model for the fine-scale turbulence noise sources in ambient jets, which is known to reproduce the G-spectrum very accurately.

In high supersonic jets additionally screech tones can occur at very distinct frequencies exhibiting high sound pressure levels (SPLs). This phenomenon also influences the two noise spectra but is generally not relevant in civil aviation, as the jet velocities are too low.

Seiner et al.¹⁸ investigated the influence of jet temperature on noise emission for a Mach 2 jet. They found that the SPL increases with increasing temperature, which is meaningful since jet velocities and thus turbulence production gain. To study the influence of temperature independently from jet velocities Bridges and Wernet⁴ compared subsonic jets at different temperatures while the velocity was kept constant. Fig. 1 depicts the noise spectra from these experiments of an ambient ($T_t = 294\text{ K}$) and a heated jet ($T_t = 534\text{ K}$). The hot jet shows higher noise levels and a stronger directivity, manifested by a narrow shape of the maximum at lower angles to the jet axis. PIV measurements of the same jets indicate that higher temperatures increase the degree of turbulence and shorten the potential core. However, the sole correction of the turbulence field only gives a slight improvement with the T&A model. Therefore, Tam et al.²³ extended their model to consider temperature effects on noise emission from fine-scale turbulence.

To determine the noise emission of more complex nozzle systems at certain observer points, empirical and semi-empirical models such as ISVR/Purdue by Tester et al.^{25,26} were developed. With increasing computational capacities numerical approaches became more interesting. These can be divided into direct and hybrid methods. For the direct method the noise sources as well as the sound propagation to the observer are calculated within a single CFD calculation. Due to the high demand on temporal and spatial discretization these methods are currently not applicable on

COMPUTATIONAL AERO-ACOUSTICS FOR HEATED AND UNHEATED JETS

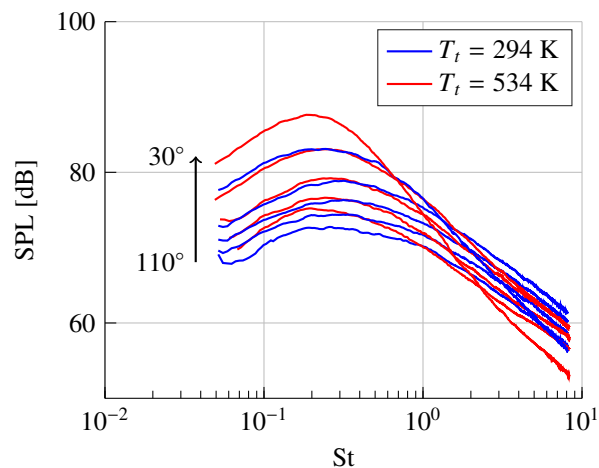


Figure 1: Temperature dependency and directivity of the ARN2 experiment

a domain enclosing the noise source region and a relevant observer point for Reynolds numbers found in a full scale engine. Hybrid approaches separate the noise generation and the propagation to reduce the computational effort. The sources can either be directly obtained from unsteady CFD simulations^{16,29} or derived from steady RANS data.^{21,23} The propagation is then calculated for a whole domain using wave equations (e.g. linearized Euler equations (LEE) or Acoustic Perturbation Equations (APE)) or evaluated at certain observer points with acoustic analogies (e.g. Ffowcs-Williams & Hawkings equations (FW&H)).

In this work, two different CAA methods are utilized to calculate the far-field noise spectra for the ARN2 experiment. To evaluate their capabilities of capturing temperature effects the two set-points shown in Fig. 1 are investigated.

The RPM method by Ewert⁶ is utilized to synthesize an unsteady pressure field from steady RANS simulations of the source region. The underlying source model is based on the afore mentioned T&A formulation. While Tam²¹ used an adjoint approach in the frequency domain, in this work the wave propagation is calculated using DLR's direct LEE-solver PIANO. Michalke¹⁰ experimentally found that only few first azimuthal modes contribute to the far-field noise. The efficiency of the RPM method is therefore based on an azimuthal-modal decomposition allowing each mode to be calculated on a separate two dimensional grid instead of a full 3-D domain. The open source code foam-extend¹ is utilized to produce the RANS results based on a $k-\epsilon$ and a RSM closure. Two total temperature based corrections are investigated to consider the afore mentioned temperature effects on the turbulence production.^{1,28}

For the second method the pressure fluctuations and their propagation in the source region are directly obtained from scale-resolving simulations (SRS). A FW&H integration of the unsteady pressure data over the time and a permeable surface enclosing the noise sources is then used to calculate the transient pressure signal at the observer points. Since SRS are very expensive, not the entire source region could be captured in this work. The permeable surface is therefore divided into multiple parts to get an estimate of the error introduced by an insufficient extent of the flow domain. The commercial CFD code ANSYS Fluent is used for both, the transient flow simulation and the FW&H extrapolation.

2. Governing Equations

In this section the governing equations for the two CAA approaches are described. For detailed information about the models used for the underlying flow simulations the reader is referred to our previous work.²⁸

2.1 RPM/PIANO

2.1.1 T&A Source Model

The fine-scale turbulence noise source model by Tam and Auriault²¹ defines a cross-correlation function for the sources depending on the mean flow and turbulence characteristics.

¹www.extend-project.de

$$\langle (Q_p)_1 (Q_p)_2 \rangle = \overbrace{\frac{\hat{R}}{\tau_s^2} \left(\frac{2}{3} \rho k \right)^2}^{\hat{R}} \times \exp \left\{ -\frac{|\xi|}{u_j \tau_s} - \frac{\ln 2}{l_s^2} \left[(\xi - u_j \tau_s)^2 + \eta^2 + \zeta^2 \right] \right\} \quad (1)$$

In this equation \hat{R} is the source variance with $A = 0.755$. ξ , η and ζ represent the distance between point 1 and 2 in three spatial directions. τ_s and l_s are turbulent time and length scale and u_j indicates the jet velocity. This model has two limitations. First, it only covers the G-spectrum, wherefore high observer angles lead to inaccurate predictions. Second, the temperature dependency is not regarded. To overcome this shortcoming Tam, Pastouchenko and Viswanathan²³ (TPV) extended the initial T&A model for hot jets.

The synthesis of the unsteady pressure field based on this model is described in detail by Ewert.^{6,13}

2.1.2 LEE Equations

The linearized Euler equations in the form proposed by Morris et al.¹¹ are applied to propagate the pressure disturbances to the far-field. First the density, the velocity and the pressure is decomposed into a mean and a perturbed part

$$\rho = \rho^0 + \rho', \quad v_i = v_i^0 + v_i', \quad p = p^0 + p'. \quad (2)$$

Assuming a constant mean flow field the linear perturbation equations read

$$\frac{\partial \rho'}{\partial t} + v_i^0 \frac{\partial \rho'}{\partial x_i} + v_i' \frac{\partial \rho^0}{\partial x_i} + \rho^0 \frac{\partial v_i'}{\partial x_i} + \rho' \frac{\partial v_i^0}{\partial x_i} = 0, \quad (3)$$

$$\frac{\partial v_i'}{\partial t} + v_j^0 \frac{\partial v_i'}{\partial x_j} + v_j' \frac{\partial v_i^0}{\partial x_j} + \frac{1}{\rho^0} \frac{\partial p'}{\partial x_i} + \frac{\rho'}{\rho^{02}} \frac{\partial p^0}{\partial x_i} = 0, \quad (4)$$

and

$$\frac{\partial p'}{\partial t} + v_i^0 \frac{\partial p'}{\partial x_i} + v_i' \frac{\partial p^0}{\partial x_i} + \gamma p^0 \frac{\partial v_i'}{\partial x_i} + \gamma p' \frac{\partial v_i^0}{\partial x_i} = Q_p. \quad (5)$$

In this case the source term Q_p on the right hand side of the pressure equation represents the acoustic sources from the T&A model and γ is the heat capacity ratio.

Applying a Fourier series decomposition along the circumferential direction to the fluctuating parts of Eqn. (3)-(5), allows the three-dimensional problem to be solved as a series of two-dimensional problems in the complex space. Each of these represents one azimuthal mode and can be solved within two calculations for the real and the imaginary part, respectively. According to experimental findings by Michalke et al.¹⁰ only the few first of these modes contribute to the far-field noise spectra. Therefore, an axis-symmetric three-dimensional case can be solved very efficiently with five to ten 2-D calculations.²

2.2 SRS/FW&H

2.2.1 Stress Blended Eddy Simulation

For the direct calculation of the transient pressure field the Stress Blended Eddy Simulation (SBES) model is used. This hybrid RANS/LES method explicitly switches between the turbulent viscosity μ_T of the RANS model near walls and the LES model in the bulk region using the shielding function f_s .

$$\mu_T^{SBES} = f_s \mu_T^{RANS} + (1 - f_s) \mu_T^{SGS} \quad (6)$$

In this work, the $k-\omega-SST$ model by Menter⁹ is used in RANS and the WALE formulation¹⁵ in LES regions.

2.2.2 Ffowcs-Williams & Hawkings Method

Ffowcs-Williams and Hawkings derived a formula to propagate the sound waves from a known source region including volume and surface sources to arbitrary observer points.⁷ It consists of a part describing the wave propagation (LHS) and one representing the acoustic sources (RHS). Spalart and Shur²⁰ found that the pressure formulation of this equation is less sensitive to errors introduced by the neglect of volume sources. This is in particular true for heated jets, when

COMPUTATIONAL AERO-ACOUSTICS FOR HEATED AND UNHEATED JETS

non-acoustic density variations occur on the FW&H surface in case of intersections with eddies. The differential form of this equation reads

$$\frac{1}{a_0^2} \frac{\partial^2 p'}{\partial t^2} - \nabla^2 p' = \frac{\partial^2}{\partial x_i \partial x_j} \{T_{ij} H(f)\} - \frac{\partial}{\partial x_i} \{[P_{ij} n_j + \rho u_i u_n] \delta(f)\} + \frac{\partial}{\partial t} \{[\rho u_n] \delta(f)\}. \quad (7)$$

$H(f)$ and $\delta(f)$ are Heaviside and Dirac functions with $f = 0$ on the FW&H surface, $f < 0$ in the region enclosed by the surface and $f > 0$ outside of it. p' is the sound pressure, a_0 is the speed of sound in the far-field, T_{ij} and P_{ij} are Lighthill's and compressive stress tensor, n_i is the unit normal vector pointing toward the exterior region, ρ is density and u_i and u_n are velocity and control surface normal velocity. If the FW&H surface is defined such that all sources are enclosed, the volume sources drop and only two surface terms remain on the RHS. The equation can then be integrated by means of the retarded Green's function. The whole procedure can be interpreted as an analogy with the divergence theorem, stating that the volume integral over a source region is equal to the integral over a surface enclosing this region.

3. Experimental Setup

The ARN2 experiment (Acoustic Reference Nozzle with $D_n = 2'' = 5.08 \text{ cm}$) was conducted at the SHJAR (Small Hot Jet Aeroacoustic Rig, Fig. 2) at the NASA Glenn Research Center. On this rig several set-points from the extensive test campaign of Tanna et al.²⁴ were reproduced using different convergent nozzles designs. Bridges and Wernet⁴ used the PIV and microphone data from these experiments to create a 'consensus' dataset including average values and an estimate of error. The noise spectra were evaluated for $15^\circ \leq \theta \leq 130^\circ$ with $\Delta\theta = 5^\circ$ and normalized to a distance of $r/D_n = 100$ using the following relation:

$$\Delta \text{SPL} = 20 * \log \left(\frac{r_1}{r_2} \right) \quad (8)$$

In this work, all spectra are additionally normalized regarding nozzle diameter and jet velocity. According to Tam and Seiner²² this gives an offset of $\Delta \text{SPL} = 10 * \log(u_j/D) = +35.3 \text{ dB}$.

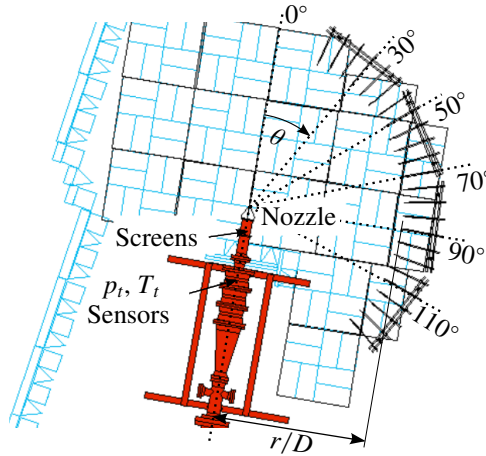


Figure 2: Experimental setup³

The two set-points detailed in Tab. 1 are chosen. They represent an unheated and a heated subsonic jet. The jet velocity is kept constant as the acoustic Mach number $Ma_a = U_j/a_\infty$ rather than the jet Mach number $Ma_j = U_j/a_j$ is relevant for noise predictions (e.g. for the Mach scaling laws). For a detailed comparison between the PIV, RANS and SRS data of these set points the interested reader is referred to our previous work.²⁸

Table 1: ARN2 experimental conditions

Case	$T_t [K]$	$p_t [Pa]$	Ma_a	Ma_j	$U_j [\frac{m}{s}]$	Re
A294	294	121257	0.050	0.51	172.1	0.6e6
A534	534	111655	0.050	0.38	171.4	0.2e6

The five microphone positions shown in Fig. 2 are evaluated. They represent side-line positions where fine-scale turbulence predominates the noise spectra ($\theta = 110^\circ, 90^\circ, 70^\circ$), a downstream position where noise from large-scale sources prevails ($\theta = 30^\circ$) and a location where both mechanisms contribute to the overall spectrum at $\theta = 50^\circ$.

4. Numerical Setup

In this section, the numerical setup of the CAA calculations is described. Here too, detailed information about the setup of the underlying RANS and SRS simulations can be found in our previous work.²⁸

4.1 RPM

Following the RPM/PIANO work-flow the first step is the derivation of non-dimensional flow and turbulence characteristics from RANS data. According to Eqn. (1) for the T&A source model these are the normalized velocity or rather the acoustic Mach number Ma_a , the time scale τ_s , the length scale l_s and the source variance \hat{R} .

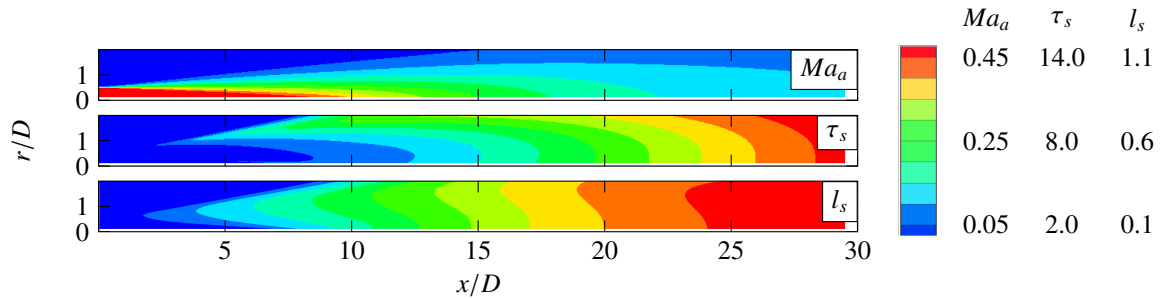


Figure 3: Non-dimensional input data on RPM patch (A294 k- ϵ)

Beside the mean velocity field, Tam used the turbulent kinetic energy k and the turbulent dissipation rate ϵ from a k- ϵ model. For second-order closures the turbulent kinetic energy is obtained from the trace of the Reynolds-stress tensor $k = 0.5\overline{u'_i u'_i}$. The non-dimensional quantities are mapped on a grid derived from stream traces. By setting the radial velocity component zero, the source patch is approximated by a rectangle to obtain uniformly distributed grid points. The patch extends $2D$ in radial and $29.5D$ in axial direction. Figure 3 depicts Ma_a , τ_s and l_s on the source domain.

4.2 PIANO

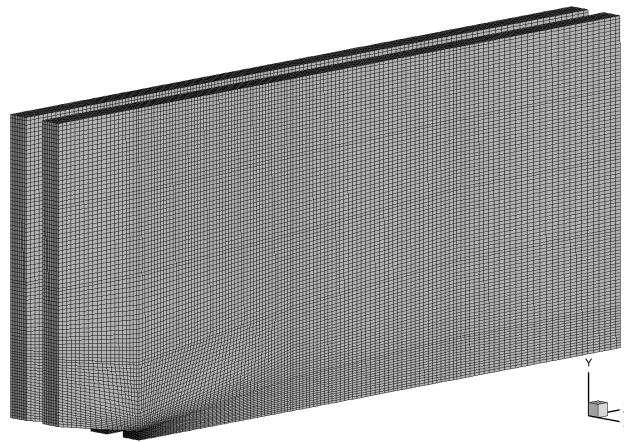


Figure 4: PIANO mesh

Due to the spatial discretization the smallest wave length to be found is resolved with seven grid points. In the source region the grid has to be further refined depending on the local acoustic Mach number. Every azimuthal mode is calculated on two single meshes, one for the real and one for the imaginary part. In this work, the first eight azimuthal

COMPUTATIONAL AERO-ACOUSTICS FOR HEATED AND UNHEATED JETS

modes are considered. To obtain smoother spectra, the zeroth and the first mode are calculated twice and then averaged. This leads to a total of ten modes. Figure 4 shows the resulting mesh with every tenth grid point plotted in axial and radial direction. It extends $15D$ in radial, $5D$ in negative and $30D$ in positive axial direction. The mesh consists of two major blocks: one for the real and one for the imaginary part. Each of these blocks consists of ten 2-D meshes for the ten modes, accordingly. In this way a total approximately seven million cells is created. Since the mesh only covers the jet and a part of the far-field, no solid walls border the domain. Therefore, all boundary conditions are chosen to be wave-transmissive. PIANO solves the LEE equations (Eqn. (3)-(5)) using a 7-point stencil finite difference scheme. For the temporal discretization a 4th-order Runge-Kutta scheme is utilized.

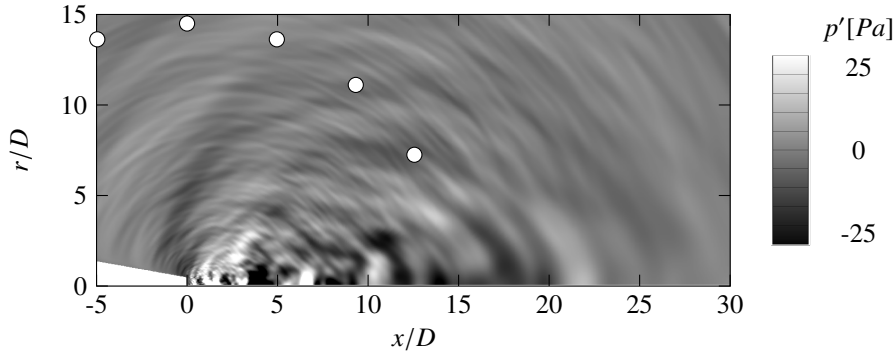


Figure 5: Instantaneous pressure field with microphone positions (A294 k- ϵ)

Figure 5 depicts an instantaneous pressure field on the whole CAA domain. Neifeld¹² showed that the application of Eqn. (8) on microphone data sampled at $r/D = 10$ leads to the same spectrum at $r/D = 100$ as extrapolated data from a FW&H surface. The CAA domain used in this work is therefore assumed to be sufficient for measurements which are not influenced by near-field effects. In Fig. 5 the five microphone positions used in this work are depicted. They are located on a circle with $r/D = 14.5$ around the point of origin.

4.2.1 SRS/FW&H

For the SRS a block-structured 360° -mesh is used. Due to the high computational costs it only covers the jet up to $x/D = 9$. The mesh consists of approximately 35 million cells. The SIMPLEC algorithm included in ANSYS Fluent is utilized to solve the transient flow equations. Both, temporal and spatial discretization are set second order.

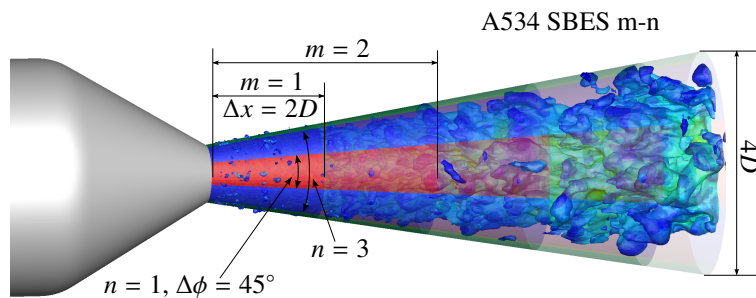


Figure 6: FW&H surface and iso-temperature surface for $T_{iso} = 330K$ (A534 SBES)

The permeable surface for the FW&H extrapolation is shown in Fig. 6 with an instantaneous iso-temperature surface at $T_{iso} = 330 K$. Since $T_{iso} - T_{\infty} \approx 0.15(T_{max} - T_{\infty})$ this surface represents the outer position of the shear layer. With a radius of $r = 2D$ at the base, the cone angle is similar to the spreading angle of the jet.

The surface is split into 40 single parts with an extent of $\Delta\phi = 45^\circ$ in circumferential and $\Delta x = 2D$ in axial direction ($\Delta x = D$ for the last circular ring, respectively). The data is separately recorded on each surface so that independent extrapolations from one or more surfaces are possible. The purpose of this segmentation is to quantify the contribution of different parts of the jet to the overall spectrum. Since each extrapolation is computationally expensive, only 9 combinations are evaluated. First the surface is stepwise enlarged in axial direction, while all parts in circumferential direction are regarded (m-n: 1-8, 2-8,...). For the investigation of the contribution in circumferential direction all

surfaces along the x-axis and an increasing circumferential number are evaluated (m-n: 5-1, 5-3,...). The whole surface mesh (5-8) consists of 120400 cells.

4.2.2 Computational Resources

Since most approaches for noise predictions are based on transient formulations, one important feature is the efficiency of a method. The azimuthal decomposition is therefore a significant advantage of the RPM simulations. Table 2 gives some information about the resources required for the A294 case.

Table 2: Computational resources

	RANS	RPM/PIANO	SRS	FW&H
time step Δt [μs]	0.165	0.295	0.500	-
initialization time ΔT_{init} [ms]	8.25	-	8.00	-
recording time ΔT_{rec} [ms]	-	22 (44)	25	-
CPU time [h] (#CPUs)	1200 (120)	3000 (39)	52000 (192)	2000 (192)
disk memory [GB]	0.25	1.0	20.0	230.0

The RANS simulation is comparatively expensive as an explicit density based solver and a 90° -mesh is utilized. Both CFD simulations need to run for an initialization time ΔT_{init} until a stationary and a quasi-stationary solution is found for the RANS model and the SRS, respectively. Even though the recording time ΔT_{rec} is nearly the same for both simulations, the RPM spectra are smoother as shown later. The reason is the doubled consideration of the zeroth and the first mode which gives a signal length of 44 *ms* instead of 22 *ms* for the subsequent Fourier transformation. The overall CPU time is approximately 13 times lower for the RPM/PIANO simulation. However, the parallelizability is limited due to mesh and processor communication requirements, so that one RPM calculation lasts about 3 days. The FW&H extrapolation requires a large disk capacity, as the transient data have to be stored on a fine surface mesh for every time step. Here too, the RPM/PIANO method is much more efficient, since the transient data only has to be stored on a 1-D microphone array for each mode.

5. Results

In the first part of this section instantaneous pressure fields in the source region of both methods are compared. Afterwards the contribution from different parts of the FW&H surface are evaluated, before the CAA data are compared to microphone measurements.

5.1 Noise Sources

To better understand the resulting spectra in section 5.3, some of the underlying source regions are regarded before. Figure 7 depicts four examples for the RPM/PIANO method and two for the SBES model. For a qualitative analysis the scales are different for the two methods but consistent within one method.

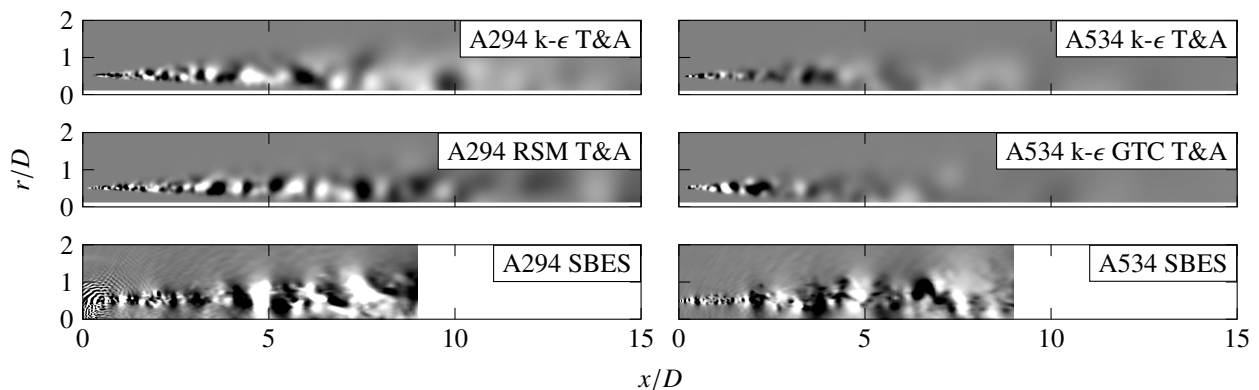


Figure 7: Instantaneous fluctuating pressure in the source region

COMPUTATIONAL AERO-ACOUSTICS FOR HEATED AND UNHEATED JETS

The upper two pictures on the left show the synthesized sources for the cold jet with the $k-\epsilon$ model and the RSM, respectively. Both fields are similar, so that no remarkable differences in the spectra are expected. The corresponding SBES field shows very strong pressure patterns at the nozzle lip. These fluctuations are considered to be a resonance problem in the numerical model. A similar behavior was found for a mixed nozzle system in our previous work.²⁷ These fluctuations are dominant up to $x/D \approx 1.5$. Between this position and $x/D = 4$ the field is similar to the RPM sources. Further downstream the scales grow faster, whereas the RPM structures develop at a constant growing rate. For the heated jet the reconstructed sources are much weaker. The reason is the formulation of the source variance in Eqn. (1) which involves the squared local density. As shown later the T&A model therefore predicts lower SPLs for the hot than for the cold jet, which is antithetical to the experimental findings. This problem can only be solved by an alternative source model formulation as from the TPV model.²³ The GTC correction leads to stronger sources and a stronger spreading rate in the initial shear layer. Interestingly the SBES of the heated jet doesn't show the unwanted perturbations. For $x/D < 2$ the scales remain very small at comparatively high amplitudes. Further downstream they quickly grow into larger structures. Here, the potential core is shorter than for the cold case so that the sources get weaker for $x/D > 7$, whereas no decay is found in the same region of the cold SBES.

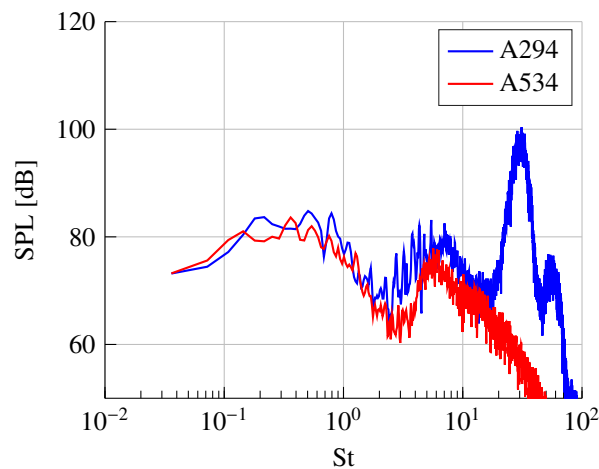


Figure 8: Unheated and heated jet (SBES 90°)

In Fig. 8 two side-line spectra for the SRS of the A294 and the A534 case are depicted. The first maximum corresponds to the G-spectrum and occurs at the expected position ($St \approx 0.3$). The second maximum is most likely caused by the open FW&H surface as discussed in the next section. The next two maxima at $St = 30$ and $St = 50$ only appear for the unheated jet and are therefore regarded as a result of the unphysical fluctuations in Fig. 7. On the one hand these maxima are far away from the frequencies of interest, on the other hand the physical maximum at $St = 0.3$ is slightly higher, while the measured spectrum is some 2 dB lower than for the heated jet. Therefore, it is not clear if this problem influences the spectrum for $St < 2$.

5.2 FW&H Surface Contributions

As section 5.1 revealed some doubts with respect to the reliability of the A294 pressure fluctuations, the investigation of the FW&H surface is conducted on the A534 data.

The left side of Fig. 9 shows the stepwise enlargement of the surface in axial direction for a side-line microphone position. As one might expect, for the 1-8 surface the SPLs in the low frequency range are low and high for higher Strouhal numbers, since the enclosed sources exhibit small scales. For $St > 1$ the selected surface seems to be rather unimportant. This can be explained by the fact that this range is dominated by sources between $x/D = 0$ and $x/D = 2$, which are enclosed by all regarded surfaces. Apart from these findings the dependencies seem to be random. A similar behavior was found by Brès et al.⁵ for heated and unheated supersonic jets: an insufficient length of the extrapolation surface leads to incorrect SPLs at low frequencies. At downstream positions the higher noise levels from instability-waves predominate this effect.

On the right of Fig. 9 the variations are remarkably weaker. An angle of 45° (surface 5-1) is obviously not sufficient but the other curves are similar. This means that the large amount of data for the extrapolation (Tab. 2) can be reduced by more than 50%.

The findings for $\theta = 30^\circ$ are mostly the same as for the side-line case (Fig. 10). On the left side for $St < 1$ it is

COMPUTATIONAL AERO-ACOUSTICS FOR HEATED AND UNHEATED JETS

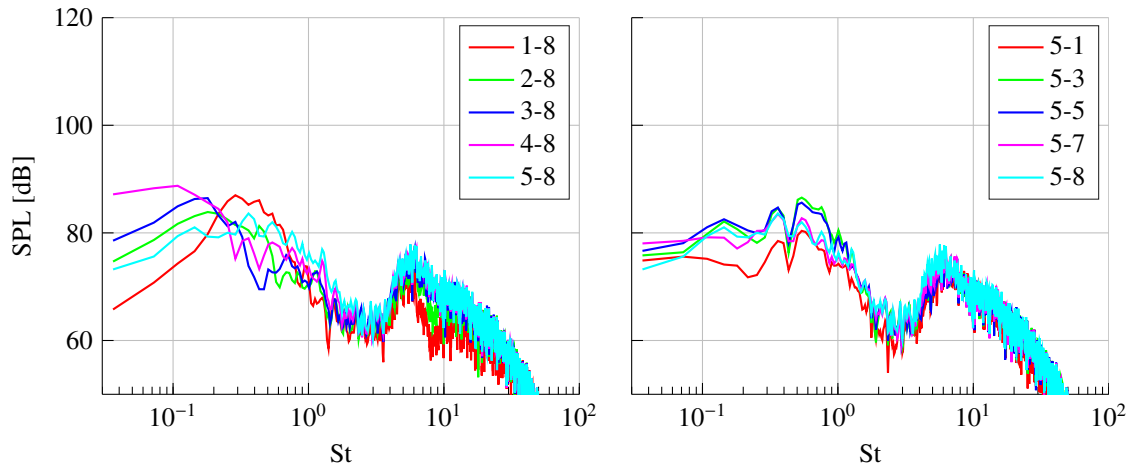


Figure 9: Axial and circumferential contributions of the FW&H surfaces for $\theta = 90^\circ$ (A534)

difficult to find a relation to the axial extent of the surface. Interestingly the unphysical local maximum shows a clear reliance: it is higher and shifted to lower Strouhal numbers for longer surfaces. This could be a hint for the origin of the maximum. In analogy with a speaker box, sources are more efficient when they are partly encapsulated. A similar situation is found at the open end of the cone where the sources are shielded while the curved surface radiates to the far-field. As the scales grow with increasing distance to the nozzle exit, the maximum is shifted to lower frequencies. An incorporation of the base area of the cone would provide clarity about this assumption. However, there is evidence that an intersection of the permeable surface with the source region leads to over-predicted SPLs.^{17,19} Therefore the cone is left open at its base in this work.

The results on the right side of Fig. 10 support the presumption that a circumferential reduction of the surface is possible.

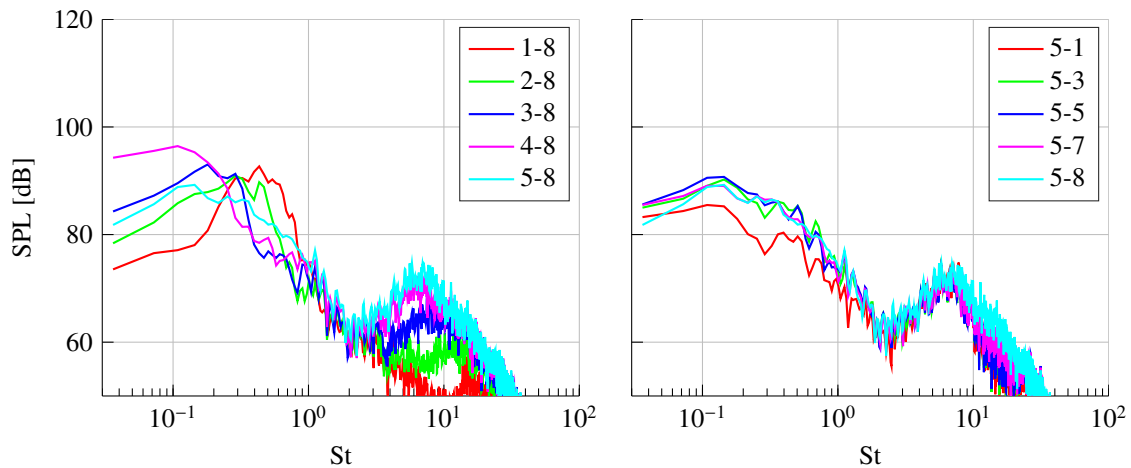


Figure 10: Axial and circumferential contributions of the FW&H surfaces for $\theta = 30^\circ$ (A534)

5.3 Noise Spectra

The CAA spectra are compared to microphone data in Fig. 11-14. For both methods the expressiveness is constrained to a certain frequency range by different limitations. The length of the recorded signal determines the smoothness of all spectra. For low frequencies a short signal can lead to a jagged shape. The doubled consideration of the first two modes minimizes the problem for the RPM/PIANO cases, but the SRS/FW&H spectra show strong variances in this area, especially for the cold jet (e.g. Fig. 12). Additionally, the limited extrapolation surface worsens this problem. At high frequencies ($St \gtrsim 2$) the SRS/FW&H data are influenced by the unphysical maxima described in section 5.1. The RANS based method is limited by the number of modes ($St \gtrsim 4$) and the mesh resolution ($St \gtrsim 8$).

COMPUTATIONAL AERO-ACOUSTICS FOR HEATED AND UNHEATED JETS

5.3.1 Unheated Jet

The side-line noise spectra in Fig. 11 show a very good agreement of the RPM/PIANO data and the experiments. These positions are dominated by noise from fine-scale turbulence, so that the model captures both, the shape of the spectrum and the position and the absolute SPL of its maximum. The difference between the $k-\epsilon$ and the RSM closure is marginal.

The SRS spectrum is some 10 dB too high. The insufficient FW&H surface is assumed to be the main reason for the offset. While the position of the maximum at $St = 0.3$ is well predicted, the shape is narrower than the expected G-spectrum.

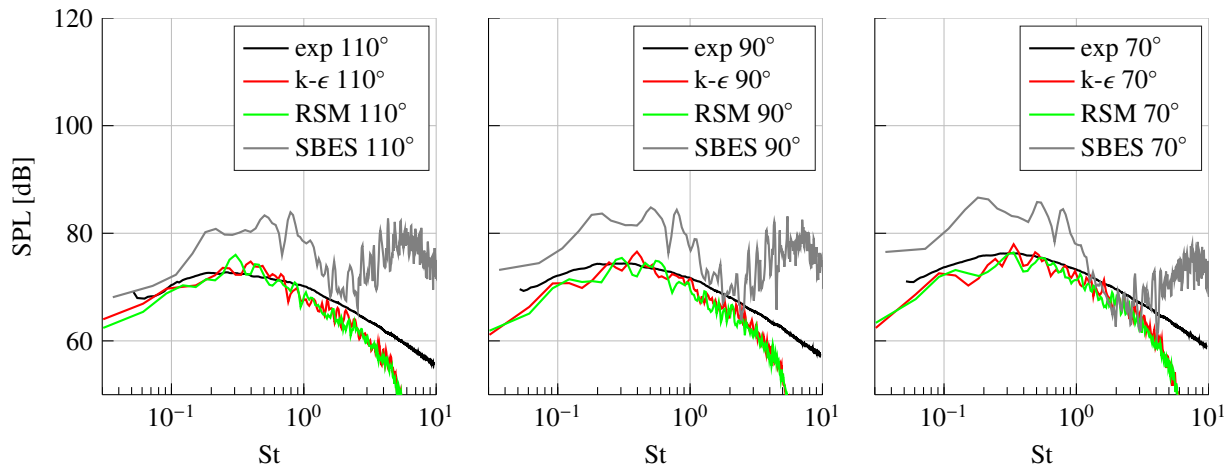


Figure 11: Side-line noise spectra (A294)

For $\theta = 50^\circ$ the measured spectrum is still dominated by the fine-scale contribution. Consequently, the synthesized sources produce very good results. As the levels are shifted upwards, the unwanted effects from the extrapolation get less dominant for $0.7 < St < 3$ in the SRS spectrum. This leads to an approximation to the experimental data in the described area and a deformation of the spectrum.

At the downstream position ($\theta = 30^\circ$) the F-spectrum is dominant. Since, the T&A model does not account for this effect, the agreement with the experimental data is worse than for the other positions. The RSM gives slightly better results than the $k-\epsilon$ model for the maximum SPL to be found. Here, the range where the SBES data fits the experimental findings reaches down to $St = 0.3$.

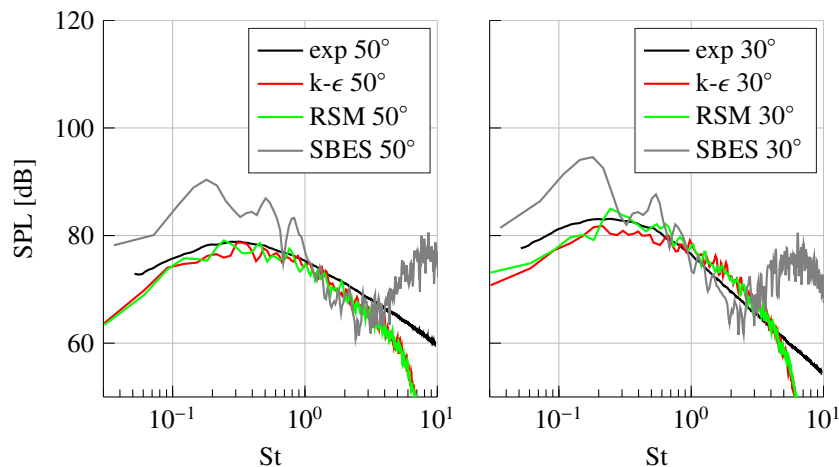


Figure 12: Downstream noise spectra (A294)

5.3.2 Heated Jet

The spectra of the heated jet draw a very different picture. The SBES results are much closer to the experiments than for the cold jet (Fig. 13). The offset is approximately +5 dB and the shape resembles the measured spectra. As the potential core is shorter for hot jets, it is assumed that the same FW&H surface better encloses the sources in this case. In contrast, the hybrid RANS/CAA method under-predicts the SPLs by some -8 dB and produces a shape resembling the G-spectrum of cold jets. The reason is, that the T&A model does not account for temperature effects. Here too, the difference between the $k-\epsilon$ model and the RSM is very small.

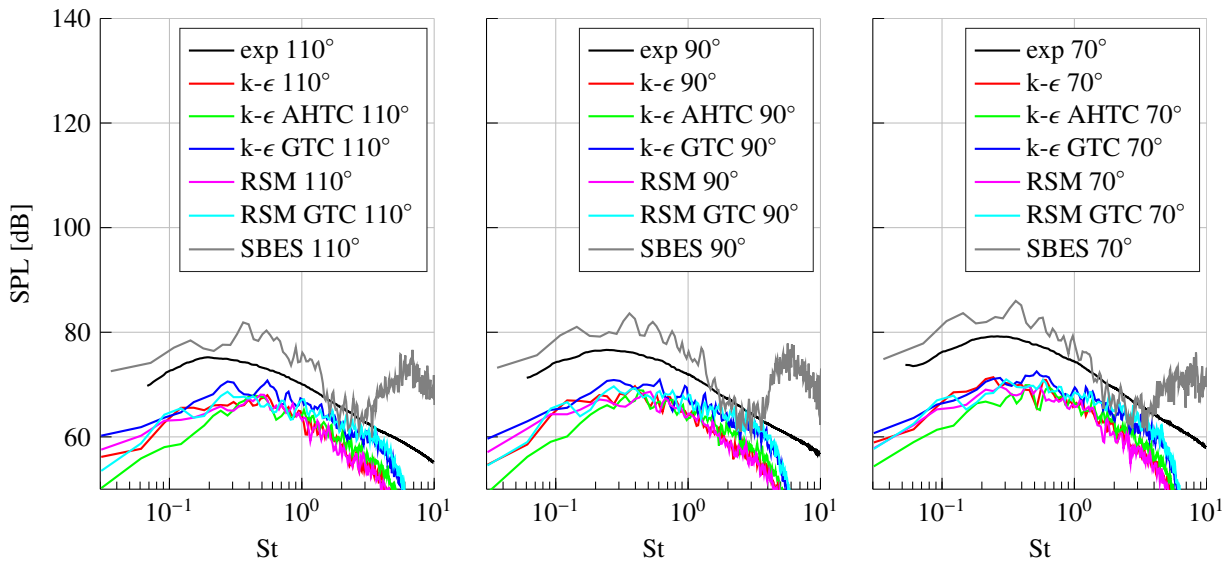


Figure 13: Side-line noise spectra (A534)

The situation is different in case of the temperature corrected models. In the low and middle frequency range ($St < 1$) the $k-\epsilon$ GTC model slightly improves the results by an offset of approximately +3 dB compared to the uncorrected counterpart, whereas the same correction hardly changes the results for the RSM. The $k-\epsilon$ AHTC model even reduces the SPL at low Strouhal numbers. For $St > 1$ all corrected models decrease the offset to the measured spectrum, in case of the GTC models to some -3 dB, for the AHTC to -6 dB from originally -8 dB of the uncorrected models.

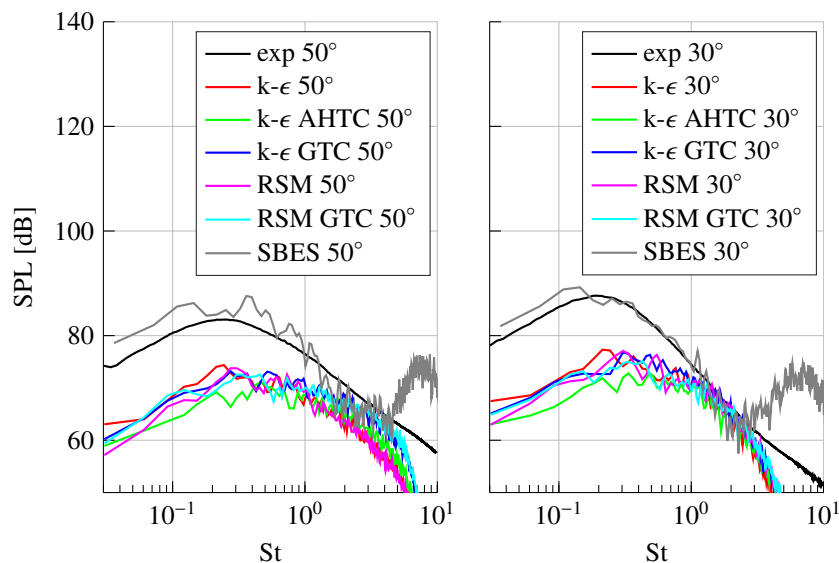


Figure 14: Downstream noise spectra (A534)

At $\theta = 50^\circ$ the SRS/FW&H approach gives very good results. The offset is minimized and the characteristic, narrow maximum of hot jets at downstream positions is well reproduced. These observations are even more obvious for

COMPUTATIONAL AERO-ACOUSTICS FOR HEATED AND UNHEATED JETS

$\theta = 30^\circ$. As the directivity is stronger for heated than for unheated jets, the offset of the hybrid RANS/CAA spectra grows up to some -14 dB with smaller angles to the jet axis.

Additional calculations with a constant dimensionless density in Eqn. 1 show stronger sources for the hot jet and thus a reduced offset in the corresponding spectra. With this modification the GTC models produce good results for $St > 1$ at sideline positions. However, the characteristic, narrow maximum from hot jets is still not well reproduced and the results of the cold jet are slightly worse as the spectrum gets narrower, so that only the results from the original T&A formulation are shown in this work.

While the behavior of the RANS/CAA model can be well explained for both, the heated and the unheated jets, the SRS results leave some open questions. For both cases the contribution of the fine-scale turbulence noise is predicted too high in the middle and low frequency range, with higher deviations in the cold case. This is most likely related to the limited extent of the FW&H surface and the fact that the dominant sources are distributed within a shorter region for heated jets.

6. Conclusion

The purpose of this work is the comparison of two different CAA approaches for the prediction of far-field jet noise. To test their capability to consider temperature effects, a heated and an unheated jet are investigated. For the SRS/FW&H method additionally the influence of different surface integration limits is studied.

In the SRS of the cold jet strong pressure fluctuations occur at the nozzle lip. They create a distinct maximum at $St=30$. As this peak does not appear in the measurements it is considered to be a numerical problem. A second maximum at $St=6$ is found in both SRS spectra. Since its position and its magnitude changes with the axial extent of the FW&H surface it is most likely related to the fact that the surface is not closed at its end. Apart from this, the segmented integration shows a strong dependency on the axial dimension and a weaker relation to the circumferential extent. The latter indicates that the amount of data processed in the surface integration can be reduced by minimizing the surface circumferentially to a segment of the axis symmetric jet. The influence of the length of the FW&H cone does not show a clear tendency in the resulting spectra.

The comparison with microphone measurements of the cold jet shows that the RPM method produces very good results for $50^\circ < \theta < 110^\circ$ with $\Delta SPL < 2$ dB. This behavior is not surprising, as the underlying T&A model was calibrated for the G-spectrum on very similar cases. At $\theta = 30^\circ$, where the F-spectrum gets dominant, the results are slightly worse. Here the RSM model produces better estimates than the $k-\epsilon$ model in the middle frequency range. The side-line spectra of the cold SRS simulation deviate from the experiments. While the position of the maximum is well predicted at $St = 0.3$, the SPL is over-estimated by about 10 dB. The reason is most likely the fact, that the permeable surface only partly encloses the source region. For downstream directions the SPLs for the middle and the high frequencies are much closer to the microphone data. At these positions the higher noise levels predominate the afore mentioned errors from the extrapolation.

The spectra of the hot jet are generally better described by the SRS/FW&H method. The shorter potential core is assumed to be the reason for this behavior. The RPM results show even lower maxima than those of the cold jet. This can be explained by the incorporation of the squared density in the source variance of the T&A model. The temperature corrected models do not remedy this problem so that another source model such as the TPV has to be used for heated jets.¹⁴ However, the GTC improves the results in the high frequency range, whereas the AHTC produces lower levels for low frequencies. For the side-line positions the SRS model over-predicts the spectra by approximately 5 dB. At lower angles the spectra get very close to the measurements.

Finally, it can be stated that the RPM/PIANO method (with the T&A formulation) produces better results for side-line positions and cold jets, whereas the SRS/FW&H approach is more accurate at downstream positions and with the heated jet. The latter is however much more expensive and shows a certain sensitivity to the choice of the FW&H surface, which leaves some doubts regarding the reliability of this approach.

7. Acknowledgement

The present work was conducted within the scope of a Munich Aerospace scholarship. Furthermore, the authors like to acknowledge Dr. Andrej Neifeld, Dr. Christina Appel, Jürgen Dierke and Dr. Roland Ewert from the technical acoustics branch of the DLR for the extensive technical support and Dr. James Bridges from the NASA Glenn Research Center for the provision of the microphone measurements.

References

- [1] Khaled S. Abdol-Hamid, S. Paul Pao, Steven J. Massey, and Alaa Elmiligui. Temperature Corrected Turbulence Model for High Temperature Jet Flow. *Journal of Fluids Engineering*, 126(5):844, 2004.
- [2] Christina Appel, Alexander Klabas, Karl-Stephane Rossignol, and Michaela Herr. RANS/CAA based Prediction of Jet Mixing Noise in Cruise Flight. American Institute of Aeronautics and Astronautics, June 2014.
- [3] James Bridges and Clifford Brown. Validation of the small hot jet acoustic rig for aeroacoustic research. In *11th AIAA/CEAS Aeroacoustics Conference*, page 2846, 2005.
- [4] James Bridges and Mark P. Wernet. Establishing consensus turbulence statistics for hot subsonic jets. In *16th AIAA/CEAS Aeroacoustics Conference*, pages 1–41, 2010.
- [5] Guillaume A. Brès, Frank E. Ham, Joseph W. Nichols, and Sanjiva K. Lele. Unstructured Large-Eddy Simulations of Supersonic Jets. *AIAA Journal*, 55(4):1164–1184, April 2017.
- [6] Roland Ewert. RPM-the fast Random Particle-Mesh method to realize unsteady turbulent sound sources and velocity fields for CAA applications. In *13th AIAA/CEAS Aeroacoustics Conference*, 2007.
- [7] John E. Ffowcs Williams and David L. Hawkings. Sound Generation by Turbulence and Surfaces in Arbitrary Motion. *Phil. Trans. R. Soc. Lond. A*, 264:321 – 342, 1969.
- [8] Michael J. Lighthill. On Sound Generated Aerodynamically I. General Theory. *Proceedings of the Royal Society of London A: Mathematical, Physical and Engineering Sciences*, 211:564–587, 1952.
- [9] Florian R. Menter. Improved Two-Equation k-omega Turbulence Models for Aerodynamic Flows. *NASA Technical Memorandum*, 1992.
- [10] Alfons Michalke. Some remarks on source coherence affecting jet noise. *Journal of Sound and Vibration*, 87(1):1–17, 1983.
- [11] Philip J. Morris and Lyle N. Long. A parallel three-dimensional computational aeroacoustics method using non-linear disturbance equations. In *Aeroacoustics Conference*, page 1728, 1996.
- [12] Andrej Neifeld. *Efficient Hybrid CAA Method for Jet Noise Prediction of Isolated Nozzles*. PhD thesis, TU Braunschweig, 2016.
- [13] Andrej Neifeld and Roland Ewert. Jet mixing noise from single stream jets using stochastic source modeling. In *17th AIAA/CEAS Aeroacoustics conference*, 2011.
- [14] Andrej Neifeld, Roland Ewert, and Marco Rose. Prediction of Hot Jet Mixing Noise Using Extended Stochastic Source Correlations. American Institute of Aeronautics and Astronautics, May 2013.
- [15] Franck Nicoud and Frédéric Ducros. Subgrid-Scale Stress Modelling Based on the Square of the Velocity Gradient Tensor. *Flow, Turbulence and Combustion*, 62:183–200, 1999.
- [16] Umesh Paliath, Hao Shen, Ravikanth Avancha, and Chingwei Shieh. Large eddy simulation for jets from chevron and dual flow nozzles. In *17th AIAA/CEAS Aeroacoustics Conference, AIAA Paper*, volume 2881, 2011.
- [17] Gilles Rahier, Jean Prieur, François Vuillot, Nicolas Lupoglazoff, and Anthoine Biancherin. Investigation of Integral Surface Formulations for Acoustic Predictions of Hot Jets Starting from Unsteady Aerodynamic Simulations. American Institute of Aeronautics and Astronautics, May 2003.
- [18] John M. Seiner, Michael K. Ponton, Bernhard J. Jansen, and Nicholas T. Lagen. The Effects of Temperature on Supersonic Jet Noise Emission. In *14th DGLR/AIAA Aero-acoustics Conference*, volume 46, 1992.
- [19] Michael L. Shur, Philippe R. Spalart, and Michael Kh Strelets. Noise prediction for increasingly complex jets. Part I: Methods and tests. *International Journal of Aeroacoustics*, 4(3):213–245, 2005.
- [20] Philippe R. Spalart and Michael L. Shur. Variants of the Ffowcs Williams - Hawkings equation and their coupling with simulations of hot jets. *International Journal of Aeroacoustics*, 8:477–492, 2009. OCLC: 781008316.
- [21] Christopher K. W. Tam and Laurent Auriault. Jet Mixing Noise from Fine-Scale Turbulence. *AIAA Journal*, 37(2):145–153, 1999.

COMPUTATIONAL AERO-ACOUSTICS FOR HEATED AND UNHEATED JETS

- [22] Christopher K. W. Tam, Michel Golebiowski, and J. Seiner. On the two components of turbulent mixing noise from supersonic jets. In *Aeroacoustics Conference*, page 1716, 1996.
- [23] Christopher K. W. Tam, Nikolai N. Pastouchenko, and K. Viswanathan. Fine-scale turbulence noise from hot jets. *AIAA journal*, 43(8):1675–1683, 2005.
- [24] H. K. Tanna, Peter D. Dean, and Robert H. Burrin. The Generation and Radiation of Supersonic Jet Noise. Volume 3. Turbulent Mixing Noise Data. Technical report, DTIC Document, 1976.
- [25] Brian Tester and Michael Fisher. A contribution to the understanding and prediction of jet noise generation in forced mixers: Part II Flight Effects. In *11th AIAA/CEAS Aeroacoustics Conference*. American Institute of Aeronautics and Astronautics, 2005.
- [26] Brian Tester, Michael Fisher, and William Dalton. A Contribution to the Understanding and Prediction of Jet Noise Generation in Forced Mixers. In *10th AIAA/CEAS Aeroacoustics Conference*. American Institute of Aeronautics and Astronautics, 2004.
- [27] Jens Trümner and Christian Mundt. Jet Noise Analysis of a Mixed Turbofan Engine. In *Internoise 2016*, 2016.
- [28] Jens Trümner and Christian Mundt. Total Temperature Based Correction of the Turbulence Production in Hot Jets. In *Proceedings of ASME Turbo Expo*, 2017.
- [29] Ali Uzun, Anastasios S. Lyrintzis, and Gregory A. Blaisdell. Coupling of integral acoustics methods with LES for jet noise prediction. *International Journal of Aeroacoustics*, 3(4):297–346, 2004.